HHS Public Access

Author manuscript

Nat Neurosci. Author manuscript; available in PMC 2017 April 10.

Published in final edited form as:

Nat Neurosci. 2016 December ; 19(12): 1665–1671. doi:10.1038/nn.4405.

Unstable neurons underlie a stable learned behavior

William A. Liberti III[1,2,*], **Jeffrey E. Markowitz**[1,*,9], **L. Nathan Perkins**[1,2], **Derek C. Liberti**[3,4], **Daniel P. Leman**[1], **Grigori Guitchounts**[5,6], **Tarciso Velho**[7,8], **Darrell N. Kotton**[3,4], **Carlos Lois**[7], and **Timothy J. Gardner**[1]

[1]Department of Biology, Boston University, Boston, Massachusetts, United States.

[2]Graduate Program in Neuroscience, Boston University, Boston, Massachusetts, United States.

[3]Center for Regenerative Medicine, Boston University School of Medicine, Boston, Massachusetts, United States.

[4]The Pulmonary Center and Department of Medicine, Boston University School of Medicine, Boston, Massachusetts, United States.

[5]Center for Brain Science, Harvard University, Cambridge, Massachusetts, United States.

[6]Program in Neuroscience, Harvard University, Cambridge, Massachusetts, United States.

[7]Division of Biology and Biological Engineering, California Institute of Technology, Pasadena, California.

[8]Brain Institute, Federal University of Rio Grande de Norte, Natal-Brazil.

Abstract

Motor skills can be maintained for decades, but the biological basis of this memory persistence remains largely unknown. The zebra finch, for example, sings a highly stereotyped song that is stable for years, but it is not known whether the precise neural patterns underlying song are stable or shift from day to day. Here, we demonstrate that the population of projection neurons coding for song in the pre-motor nucleus HVC change from day to day. The most dramatic shifts occur over intervals of sleep. In contrast to the transient participation of excitatory neurons, ensemble measurements dominated by inhibition persist unchanged even after damage to downstream motor nerves. These observations offer a principle of motor stability: spatio-temporal patterns of inhibition can maintain a stable scaffold for motor dynamics while the population of principle neurons that directly drive behavior shift from one day to the next.

Correspondence should be addressed to Timothy J. Gardner, timothyg@bu.edu.

*Equal Contribution Statement

These authors contributed equally to this work

[9]Present address: Department of Neurobiology, Harvard Medical School, Boston, Massachusetts, United States.

Author Contributions

WAL, JEM, GG, and DPL performed the experiment; JEM and WAL analyzed the data; LNP provided software for the custom microscope; DCL, DNK, TV and CL provided the lentivirus; WAL, JEM and TJG designed the experiment and wrote the manuscript.

Introduction

Questions about coding stability at the single neuron level have been notoriously difficult to address given the challenge of stably recording from single neurons using implanted electrodes. In the hippocampus, earlier methods tracking tens of cells emphasized stable neural tuning over a timescale of a week [1,2], whereas recent studies tracking thousands of cells using new optical techniques [3,4] revealed that 75–85% of the cells change their tuning properties within the same timeframe [5]. In whisker motor cortex, individual neurons in mice trained on an object detection task were unstable, but the relationship between ensemble measurements and behavior remained stable [6]. These studies support the view that for stable behaviors, individual neurons involved can show substantial drift in their tuning properties.

For motor systems, the stability of neural tuning is not necessarily expected– the convergence of vast numbers of neurons in motor cortex to relatively few muscles [7] suggests that a given muscular activation pattern could be produced by many patterns of neural activity [8]. In parallel, single neurons in motor cortex are observed to switch tuning properties in a task-dependent manner [9]. In the case of the zebra finch, the precise timing and acoustic structure of song is preserved for years [10,11]. Since the zebra finch sings a single song over the course of his lifetime, the question of neural coding stability is particularly well-defined. In the pre-motor nucleus that drives song, HVC (used as a proper name), three primary classes of neurons can be found: inhibitory interneurons, basal-ganglia projecting neurons (HVC_X), and motor projecting neurons (HVC_RA). A third projection neuron type HVC_AV sparsely populates the nucleus, but its activity has not yet been described in singing birds [12]. In HVC, each neuron type that has been observed produces a highly stereotyped pattern of action potentials, and these patterns are stable over the time intervals that they have been recorded: minutes to hours [13,14]. For inhibitory interneurons, the pattern is dense, with spikes occurring throughout song [14,15]. In contrast, excitatory projection neurons that communicate with downstream targets fire “ultra sparsely” [13].

During song production, HVC_X neurons and inhibitory interneurons exhibit cell-type specific phase-locking to the local field potential (LFP) at 30 Hz. HVC_X cells fire in the peak of the LFP and interneurons in the trough [16]. Intracellular recordings in vitro and in vivo suggest that HVC_RA neurons also fire in gaps of inhibition [17]. Moreover, both the LFP and projection neuron activity are clustered over a 100 μm length-scale. The phase locking relationship between excitatory and inhibitory neurons is only observed with multiple neuron recordings in the same small volume– phase shifts across HVC preclude a global rhythmic relationship among cell types [18]. Taken together, these observations indicate that spatially coherent mesoscopic patterns of inhibition underlie HVC dynamics, where synchronous gaps in local interneuron population activity control projection neuron timing.

The recent evidence in support of locally organized ensemble activity in HVC allows us to raise the following question: What explains the persistence of the song motor pattern, single neuron stability, or stability of ensemble dynamics? A recent experiment suggests that HVC ensemble dynamics measured through multi-unit activity [19] are resilient to circuit perturbations [20]. Here we extend the observation of HVC ensemble dynamics using new

electrophysiological [15] and imaging methods (Fig. 1) to address the stability of excitatory projection neurons.

Results

Song is supported by stable mesoscopic dynamics

Local field potentials (LFPs) can reflect the synchronous activity of neural ensembles over a length-scale of approximately 100 μm [21] (though see [22]). We recorded LFPs in the zebra finch pre-motor nucleus HVC using both commercial and previously-described custom carbon fiber electrode arrays [15,16] (see **Methods**). The phase of the 30 Hz LFP is coherent with the spiking of HVC interneurons and projection neurons (Fig. 2a–f) [16]; we found this local phase was precisely conserved over long timescales (Fig. 2g). For most of our implants we were able to record the LFP for up to 30 days, and we found that over this timescale the 30 Hz phase exhibited a drift of less than 0.25 radians or approximately 15 degrees (modal change of .244 radians over 30 days, .232–.254, 95% bootstrap confidence interval, Supplementary Figure 1a). This stability in LFP phase indicates that ensemble activity, reflecting a combination of local spiking and presynaptic inputs, does not undergo a major reconfiguration.

Multi-unit ensembles and single inhibitory neurons are stable

The LFP is thought to reflect ensemble activity from both excitatory and inhibitory neurons over a length-scale of approximately 100 μms [16], similarly, multi-unit recordings can reflect the aggregate activity of tens of nearby neurons within a local volume. To monitor the stability of multi-unit activity, we implanted bare carbon fibers with a length matched to the full depth of HVC (see **Methods**). Fig. 2h reveals a multi-unit raster with detailed temporal structure in the pattern of firing and silence, with an average precision of 4.587 ms (4.348–4.843 ms, 95% bootstrap confidence interval, see **Methods**) consistent with the stereotyped neural activity reported previously in HVC [13,23]. The neural patterns shown in Fig. 2h represent finely timed bursts of activity in an unknown number of cells (the number of simultaneously active cells recorded per electrode was more than could be separated by spike-sorting). However, spike-field measurements indicate that, as for single inhibitory neurons, the multi-unit signal is phase-locked to the trough of the 30 Hz component of the LFP. This suggests that the multi-unit signals are dominated by inhibitory interneurons (Fig. 2c,f) [16]. Enhanced representation of inhibitory cell activity in multi-unit signals is to be expected since projection neurons fire “ultra-sparsely” [13] and contribute many fewer spikes to a multi-unit signal than do interneurons. The suggestion drawn from multi-unit signals that patterns of inhibition are stable in HVC (Fig. 2h–j) was directly confirmed in long-term single unit recordings from n=6 inhibitory neurons from single unit recordings (3 are shown in Fig. 2k). As revealed in Fig. 2k, inhibitory neuron firing patterns were remarkably stable, even over a time-scale of months. In addition to the stability of the 30 Hz LFP phase, this result indicates that ensemble inhibitory activity is highly stable.

We next asked if the stability of this multi-unit activity depended on sensory feedback. Previous work has shown that the statistical distribution of post-synaptic potentials (PSPs) in HVC projection neurons is invariant to altered auditory feedback induced through a

tracheosyringeal (TS) nerve cut [24], but over long timescales, the song of the adult zebra finch is known to be maintained through an auditory-feedback dependent process [25,26]. We anticipated that the rate of drift in the ensemble pattern could increase with perturbations to auditory feedback. Following baseline recording, we severed the ipsilateral TS nerve that relays motor commands to the birds' vocal organ (n=5 birds, see **Methods**). As in previous work [24,27], this loss of muscular control results in acoustic distortions of song (Fig. 3a–d, see Supplementary Figure 2 for all examples), degrading the learned sensory-motor correspondence between vocal commands and auditory feedback. Following this, we monitored the song and HVC multi-unit firing patterns for a period of approximately one month. Over this time interval, song did not recover, and the multi-unit spike patterns in the pre-motor nucleus HVC remained stable (Fig. 3e–f). In all birds subject to the TS cut, shifts in the firing pattern occur at the same rate as for baseline recordings ($p>.05$ for all birds, one-tailed Wilcoxon rank-sum test, see **Methods**). We conclude from this that the ensemble pattern in HVC is robust to changes in auditory feedback that result from unilateral TS nerve removal. Here the song is altered, but the detailed ensemble firing patterns persist in HVC as though no change had occurred. This observation is synergistic with a recent study showing resilience of the HVC ensemble pattern after neural circuit perturbations [20].

Individual projection neurons are unstable over days

Our electrophysiology methods were typically unable to track individual excitatory projection cells over time-scales longer than a single day, perhaps due to limitations of recording from smaller cells [15]. To provide information about the stability of excitatory cells, we turned to optical imaging of genetically encoded calcium indicators (Fig. 4a, Supplementary Figure 3, see **Methods**) [16,28] using a virus that labels excitatory projection neurons in HVC but does not label inhibitory neurons (see **Methods**). Imaging during singing was accomplished through the use of miniature head-mounted microscopes [3] using both a commercial head-mounted microscope (Inscopix, n=1 bird), and a custom 3D–printed microscope (n=3 birds) designed to promote freedom of movement in singing birds (Fig. 4 and Supplementary Figure 4, see **Methods**). The custom microscope provided the first measurements of calcium activity during undirected singing–the solo practice song of the zebra finch. Projection neuron calcium activity patterns were sparse and time-locked to singing (Fig. 4a). The timing of most projection neurons was stable over several days (Fig. 5a,b), however, across days, the probability that a given cell fires during singing can change dramatically (Fig. 5c, Supplementary Figure 5). Across an interval of days, cells both drop out and newly appear in the song pattern (Fig. 5b,c, and Supplementary Figure 6–8). Stable and unstable ROIs can be found next to each other (Fig. 5c and Supplementary Figure 6,7).

One class of projection neuron (HVC_X) can produce more than one time-locked burst of action potentials during singing. For cells with multiple timing peaks, amplitude or probability of activation could change independently for each peak. This was observed both in calcium imaging and in electrophysiological recordings, where we have witnessed the 'fade-in' of a second burst time in a projection neuron recorded with a carbon fiber electrode over the course of a day (Fig. 5d).

For the imaging data, we performed analysis on two ROI sets: one analysis included all ROIs found on any day of imaging ($ROIs_{present\ some\ days}$). The second included only ROIs unambiguously present on *all* days of imaging ($ROIs_{present\ all\ days}$). By the fifth day of imaging, across all ROIs recorded, a large number of ROIs showed statistically significant changes in their mean song-aligned activity ($p<.01$ permutation test, 15/39 ROIs for bird 1, 27/38 for bird 2, 26/76 for bird 3 and 26/81 for bird 4, $ROIs_{present\ some\ days}$; 11/18, 14/16, 11/22, 5/21, $ROIs_{present\ all\ days}$).

The shift in projection neuron activity across multiple days contrasts with our electrophysiological recordings, which typically revealed stability of projection firing patterns over the course of hours within a single day [13,15,29] (Fig. 6a,b). This contrast motivated us to examine whether the shift in projection neuron activity occurred over intervals of sleep (Fig 6c–f). We found a much stronger shift in song-aligned projection neuron calcium traces after a night of sleep than over the course of a single day (Fig. 6c, Supplementary Figure 6, $ROIs_{present\ some\ days}$ p=2.0e-40, z=−13.26, $ROIs_{present\ all\ days}$ p=1.6e-14, −7.59, one-tailed Wilcoxon signed-rank test). Next, we checked if drift could be accounted for by time elapsed. First, we analyzed whether calcium activity decreased in consistency across the day, and, surprisingly found the opposite to be true: consistency *increased* over the course of each day (Fig. 6e, $ROIs_{present\ some\ days}$ r=.14 p=6.1e-9, $ROIs_{present\ all\ days}$ r=.18, p=9.7e-7, see **Methods**). We also found that song-aligned calcium activity became more similar to the previous day's average over the course of the day (Fig. 6f, $ROIs_{present\ some\ days}$ r=.12, p=5.6e-3, $ROIs_{present\ all\ days}$ r=.25 p=4.3e-9, Spearman rank correlation). Thus, calcium traces in single cells change both their mean pattern and variance overnight, and then return toward the previous day's average as the day progresses, while at the same time becoming more stereotyped. Given these observations, the drift in calcium activity is not simply a function of time elapsed. Rather, these results suggest that sleep actively destabilizes the representation of song in pre-motor nucleus HVC.

The microstructure of song changes overnight and increases in consistency throughout the day

The finding that projection neuron activity is unstable across days prompted us to examine the microstructure of song behavior using a highly-sensitive time-frequency analysis method developed for analysis of sparse signals, such as zebra finch song (see **Methods**). The persistence of zebra finch song structure has been documented over timescales of years [10,11] and as demonstrated in Fig. 1, over the period of a year, the song appears to be remarkably stable (Fig. 1A); however, the micro-structure of song is not precisely the same, even in this example. High resolution investigation of the microstructure reveals small but significant shifts over the interval of a week, and these changes occur primarily over periods of sleep (p=9.8e-4 w=55, one-tailed Wilcoxon signed-rank test n=10 similarity scores for n=10 birds, Supplementary Figure 9, see **Methods**). Moreover, similar to the drift in calcium activity, we found that song consistency also increases over the course of the day (Fig. 6d, r=.28, p=6.6e-8, Spearman rank correlation, see **Methods**).

Discussion

This study suggests motor skills encoded in the brain, like many structural features of the human body, undergo renewal at the cellular level. Skin maintains its shape despite the turnover of cells [30], and the intestinal surface has constant turnover but maintains its function [31]. For the stable song of the zebra finch, instability of the neural program qualitatively matches the microscopic day-to day changes in song, but the song changes observed over intervals of sleep are small, while the pattern of neuronal participation changes more dramatically. What explains the persistence of the song motor pattern in spite of the unstable projection neurons underlying song?

A key finding is that on a mesoscopic scale, the pre-motor nucleus HVC is stable. Over the length scales recorded in LFPs and multi-unit recordings (approximately 100 microns), the neural basis of song is largely unchanged over a timescale of weeks to years. In contrast, individual projection neurons drift–not primarily in the timing of their activity, as much as in the burst probability and participation in the song pattern. One potential factor contributing to ensemble stability in HVC is the spatial correlation observed in the firing patterns of excitatory cells. Nearby excitatory neurons in HVC fire at similar times, and the length-scale of this correlation is roughly 100 microns [16]. If individual projection neurons fade out of the ensemble, nearby projection neurons could be serving redundant roles.

A second related factor contributing to ensemble stability is the role of temporally patterned inhibition in HVC. In contrast to the instability of excitatory neuron coding, we have observed that inhibitory interneuron firing patterns are stable for weeks or months–for as long as it was technically possible to track the firing patterns of the cells. At the simplest level, excitatory neurons are postulated to be driven by a relatively sparse number of strong synapses, leading to the sparsity of their firing patterns [29,32] In contrast, many inhibitory interneurons in HVC have large dendritic arbors and are thought to be driven by a large number of presynaptic partners [33]. The prediction from HVC connectivity is that changes in a small number of synapses could alter the excitatory neuron firing patterns dramatically, but influence the inhibitory interneurons very little. In light of this numerical argument, and the observed stability of single inhibitory neurons, HVC ensemble patterns could be stabilized if interneurons have a strong local influence over projection neuron activity. Indeed, this appears to be the case. The firing times of the excitatory projection neurons coincide with stereotyped pauses in local inhibition [17,34], and HVC_X excitatory neurons and inhibitory interneurons fire in opposite phases of the 30Hz LFP [16]. The observations are true on the micro-scale, and due to phase shifts across the extent of HVC the rhythmic alternation is not observed globally [18]. Local blockade of inhibition releases the sparse firing cells from inhibition and they begin to fire at multiple times in song [17]. Building on these observations, a recent modeling study suggested that inhibitory interneuron dynamics can increase the robustness of HVC dynamics to added noise [35]. These models can be made more precise in future experiments as additional cell-type specific information is measured. The relative stability of different classes of HVC excitatory neurons (HVC_RA, HVC_X and HVC_Av) remain to be examined since our methods could not distinguish among the three cell types. In the songbird, stable patterned inhibition may be an important force in maintaining the dynamical pattern of song in spite of underlying drift in the projection neurons. For

mammals, similar principles may apply. Aspects of the song cortico-thalamic loop resemble features of mammalian motor cortex, including an important 30 Hz rhythm [16,36,37] and spatial correlations in neuron firing patterns over 100 μm length scales [38–40]. In mammalian motor cortex, it will be interesting to track drift in excitatory versus inhibitory neuron populations to see if patterned inhibition may provide a stabilizing force in motor skill persistence.

Finally, we address the importance of sleep in the rearrangement of the song code in HVC. The change in the song motor pattern occurs primarily over intervals of sleep, and we have shown that adult song behavior also undergoes microscopic shifts in sleep. Our results may be related to a previous observation: as juveniles learn to sing, their songs progress through a day of practice [41], but degrade slightly over intervals of sleep [42]. The depth of this overnight "backsliding" is positively correlated with the eventual success of song learning–indicating that nighttime song rearrangements are important for learning. In addition, if song-aligned HVC activity is disrupted through lesioning Nif, an area upstream of HVC, the pattern recovers primarily overnight [20].

The present study provides a possible neural mechanism for these sleep effects, raising the possibility that new patterns of activity "invented" over intervals of sleep provide important raw material for song learning and maintenance. Francis Crick proposed that noisy reactivation of neural circuits in sleep weakens the strongest pathways in the brain, promoting adaptive plasticity [43]. It is thought that in sleep, songbirds reactivate their song patterns in the motor region RA in a noisy or incomplete manner [44] and it is possible that this spontaneous activity drives the overnight shift in HVC excitatory neurons observed here. Future studies can track the firing patterns of excitatory neurons in HVC while silencing or over stimulating spontaneous activity in sleep, directly testing the hypothesis that noisy replay of song in sleep promotes adaptive plasticity of the song motor program. It also remains to be seen whether the overnight shift in HVC is random, or guided by vocal errors. Random shifts in the population could increase robustness of HVC dynamics by enforcing redundant representations of song. In contrast, shifts in the population that are influenced by vocal performance errors could be an active part of song learning and maintenance.

Methods

Subjects

All procedures were approved by the Institutional Animal Care and Use Committee of Boston University (protocol numbers 14-028 and 14-029). Electrophysiology data were collected from n=27 adult male zebra finches (>120 DPH), and imaging data were collected from n=4 adult male zebra finches. Birds were individually housed for the entire duration of the experiment and kept on a 14 h light-dark cycle. The birds were not used in any other experiments.

Splaying microfiber electrodes

We used a previously-described minimally invasive carbon fiber electrode array [15] in addition to commercially available arrays (TDT, Neuronexus) to chronically monitor both

single units and LFPs. Extracellular voltages were amplified and digitized at either 25 or 30 Khz using the Intan acquisition system (RHA2000 and RHD2000).

Microfiber electrodes for multi-unit recordings

Bare (i.e. uncoated) microthread electrodes were prepared by extracting 5 and 11 μm diameter fibers from commercially available spools of carbon fiber (grade XAS, HTA, T300 or P25). Once extracted, sizing and other impurities were removed by heating fibers as previously described [15]. The bare fibers were then attached to coated silver wire using a conductive silver paint (842-20G, MG Chemicals). Signals were sent from a custom headstage to a differential amplifier (AM Systems 1700, gain of 1000, low cut-off 300 Hz, high cut-off 5 kHz), and digitized with a National Instruments Acquisition board (PCIE 6323, 40 kHz sampling rate).

Tracheosyringeal nerve cut

The right TS nerve was removed using previously described methods [27]. Briefly, birds were anesthetized with 4% isoflurane and maintained at 1–2% for the course of the surgery. Feathers were removed from the neck, and an incision was made over the trachea. The nerve was dissected from the surrounding tissue and the nerve was pulled from its roots on the syrinx, extracting a minimum of 1 cm of nerve length.

Calcium imaging

To image calcium activity in HVC projection neurons during singing, we employed head-mounted fluorescence microscopes–both commercial and custom built. This method provides long-term recordings of calcium signals in HVC [16], and enables studies of motor stability and adaptive plasticity at the single neuron level. For viral delivery, we use the genetically encoded calcium indicators GCaMP6s (2 birds) and GCaMP6f (2 birds) delivered by lentiviruses [16,45].

For 1 bird, we used a commercial microscope (Inscopix) to gather female-directed singing over 5 day periods. However, these microscopes could not be used with a rotary commutator and were too heavy to evoke reliable undirected or solo song. Motivated by these challenges, we developed a light-weight (1.7g), commutable, 3D printed single-photon fluorescent microscope that simultaneously records audio and video Fig. 4, Supplementary Figure 4 (n=3 birds). These microscopes enabled recording of hundreds of songs per day (all birds sang at least 500 songs on at least one day of recording), and all songs were recorded from birds longitudinally in their home cage, without requiring adjustment or removal of the microscope during the imaging period. Birds were imaged for less than 20 minutes total on each imaging day, and LED activation and video acquisition were triggered on song using previous described methods. All analysis was restricted to a particular bout in song, either the first (1 bird) or the second (3 birds). Recordings were taken from 3 weeks to 3 months post-injection.

Microscope design

The custom microscope is similar to a previously described design [3] (Fig. 4, Supplementary Figure 4). A blue LED produces excitation light (470nm peak, LUXEON Rebel). A drum

lens collects the LED emission, which passes through a 4 mm × 4 mm excitation filter, deflects off a dichroic mirror and enters the imaging pathway via a 0.25 pitch gradient refractive index (GRIN) objective lens. Fluorescence from the sample returns through the objective, the dichroic, an emission filter and an achromatic doublet lens that focuses the image onto an analog CMOS sensor with 640 × 480 pixels mounted on a PCB that also integrates a microphone. The frame rate of the camera is 30 Hz, and the field of view is approximately 800 μm × 600 μm. The housing is made of 3D printed material (Formlabs, Black resin). A total of 5 electrical wires run out from the camera—one wire each for camera power, ground, audio, NTSC analog video, and LED power. These wires run through a custom flex-PCB interconnect (Rigiflex) up to a custom-built active commutator, based on previously described designs [46]. The NTSC video signal and analog audio are digitized through a USB frame-grabber. Custom software written in the Swift programming language running on the Mac OS X operating system (version 10.10) leverages native AVFoundation frameworks to communicate with the USB frame-grabber and capture the synchronized audio-video stream. Video and audio are written to disk in MPEG-4 container files with video encoded at full resolution using either H.264 or lossless MJPEG Open DML codecs and audio encoded using the AAC codec with a 48 kHz sampling rate. In addition, the software communicates with a microcontroller via a USB-to-serial connection to manipulate LED intensity, and samples a trigger signal from a DSP performing song detection (TDT RX8), in order to selectively record during singing.

Virus Information

Addgene plasmids # 40753 (pGP-CMV-GCaMP6s) and # 40755 (pGP-CMV-GCaMP6f) (gift of the Douglas Kim Laboratory) were transformed into E.Coli bacteria by heat shock, and sequenced. The GCaMP6s and GCaMP6f fragments were PCR amplified with the addition of NotI/BamH1 to the 5' and 3' ends respectively. GCaMP6s was cloned into the pHAGE-CMV-eGFP vector to form pHAGE-CMV-GCaMP6s. The RSV promoter sequence was ordered from IDT as a gblock with the addition of SpeI/NotI to the 5' and 3' ends respectively and was cloned into pHAGE-CMV-GCaMP6s and pHAGE-CMV-eGFP to form pHAGE-RSV-GCaMP6s and pHAGE-RSV-eGFP. GCaMP6f was then cloned into pHAGE-RSV-GCaMP6s to form pHAGE-RSV-GCaMP6f. The viruses were packaged in HEK 293T cells and titered on FG293 cells, with titers ranging between 1.2–2.3 × 10^10 infectious particles/mL. Plasmid maps and sequences of all lentiviral vectors employed can be downloaded from the vectors page of the laboratory of Darrel Kotton: www.kottonlab.com. These plasmids have also been deposited for distribution on addgene: www.addgene.com/Darrell_Kotton plasmid ID #80315 and #80146.

The tropism of our virus for excitatory neurons was evaluated by counterstaining using known markers of inhibitory neurons, specifically Anti-Parvalbumin (Abcam Ab11427), Anti-Caretinin (SWANT 7697), and Anti-Calbindin (SWANT CB-300). All observable GCaMP6 labeled dendrites contained spines, consistent with the morphology of HVC_RA and HVC_X projection neurons. Out of 1000 counted neurons, only 1 was double-labeled with inhibitory markers. Confocal imaging of GFP-positive cells revealed that in all cases where dendrites were visible they contained spines, consistent with the known morphology of HVC_{RA} and HVC_{X} projection neurons. The morphology of all GFP-positive cells was

consistent with previous descriptions of projection neurons in HVC, but not consistent with either glial cells or inhibitory neurons. Our histology also revealed dense axon arbors in nucleus RA, and Area X, indicating that a significant number of HVC_{RA} and HVC_X neurons were labelled (Supplementary Figure 3). The combined weight of these observations suggests that lenti-RSV overwhelmingly labels projection neurons in HVC. However, it remains unclear if the excitatory neuron tropism results from the RSV promoter, or if it is a general tropism of the lentivirus construct itself, or a combination of both.

Data Analysis

Song alignments—Songs were aligned using the Euclidean distance in spectral features between the data and a template song in a sliding window. Local minima in the Euclidean distance were considered candidates hits, which were then plotted in 2 dimensions for the user to perform a cluster cut. No time warping was applied to any data. These methods have been described in more detail previously [47].

Spectral density images—To plot the variability of multiple song renditions in time and frequency we used the spectral density image, which has been described previously [16,48]. A sparse binary time-frequency representation was generated using auditory contours [49,50]. These time-frequency binary images were combined by averaging across all renditions. In the resulting image, the value at each pixel is the probability that a time-frequency contour passes through it.

Acoustic change post-nerve cut—To analyze the change in song post-TS nerve cut, we computed amplitude modulation (AM), frequency modulation (FM), Wiener entropy, amplitude envelope, pitch and pitch goodness using Sound Analysis Pro for MATLAB [51]. We then computed the average or variance of each feature across the entire song and compared the last day of singing pre-cut with the first day of singing post-cut.

Acoustic change overnight—To quantify changes in song microstructure we used the similarity score derived from the spectral density image, which has been described previously [48]. For 5 consecutive days of singing from n=10 birds, we divided each day's worth of singing in half by trial number. To compute the change in song microstructure across the day, we computed the similarity scores between trials from the first half of the day and the spectral density image from the second half of the day. Then, to analyze the overnight change we computed similarity scores between trials from the first half of each day and the spectral density image from the previous evening. Finally the scores were averaged for each day prior to statistical comparison. Next, to estimate the change in song consistency over the course of the day (Fig. 6d), we computed the spectral density image for each hour's worth of singing. Then, similarity scores were calculated for each trial and the corresponding spectral density image. Values were averaged in 1 hour time bins. Trends were estimated by taking the Spearman rank correlation between similarity score and the time of day.

Local field potentials and single units—Local field potentials (LFPs) were analyzed as described previously [16]. Extracellular voltage traces were median filtered (1 ms window)

to remove spikes and then lowpass filtered with 400 Hz corner frequency (4th order Butterworth filter) and downsampled to 1 kHz. Finally, the LFP was filtered with a 25–35 Hz bandpass (8th order Elliptic filter for Fig. 1; 53 tap Kaiser window FIR filter, 20 dB stopband attenuation, .05 ripple for all analysis to minimize the impulse response). To compute the change in phase angle, we used the angle of the Hilbert-transformed narrowband LFP.

Single interneurons were analyzed as described previously [16]. Extracellular voltage traces were band-pass filtered from 600-11 kHz (12th order Elliptic filter, .2 dB passband ripple, 40 dB stopband attenuation) and sorted using standard offline spike sorting techniques [52,53].

Multi-unit electrophysiology—First, threshold crossings were taken from extracellular traces digitized at 40 kHz using a threshold of 2.5 robust standard deviations [54]. Threshold crossing were then converted into firing rates on a single-trial basis by convolving with a Gaussian kernel (5 ms sigma). Alternatively, the root-mean-square (RMS) of the voltage signal was calculated in a 5 ms sliding window (box car). To estimate the stability of multi-unit activity, we averaged either the song-aligned firing rate or RMS across all trials in a given day. Then, the Pearson correlation coefficient was computed between the averages from either the first day of recording (or the last day pre-TS cut) and each subsequent day (Fig. 2i–j). To compare the drift post-TS cut to the baseline condition, correlation values were binned in a 16 day sliding window (5 day overlap, the result was insensitive to binning parameters, data not shown), and a bootstrap test was performed between the binned pre- and post-nerve cut correlation values (Fig. 3e–f). That is, binned post-nerve cut values were compared with 1,000 bootstrap estimates of the corresponding pre-nerve cut correlation values. Exact p-values were (from smallest to largest, both spikes and RMS), p=.075, .11, .22, .42, .58, .74, all others p=1.

Calcium imaging—Time plots used in Fig. 5a were created by averaging all song-aligned calcium imaging movies for a bird within a single day. The resulting ‘average' movie was smoothed with a 15 μm gaussian filter, and each pixel was then colored by its center of mass in time. To create presence or absence images used in Fig. 5c, Maximum projection images were created for all song-aligned calcium imaging movies, and the average pixel intensity of these maximum projections was taken for each day of imaging. Each day is mapped to the red, green, or blue. For Supplementary Figure 7c, each maximum projection image is divided by a smoothed version of the same image, using a 100 μm pixel disk filter, to normalize across bright and dim ROIs.

Region Of Interest (ROI) based analysis was performed as described previously [16]. In brief, raw imaging data was motion corrected using a previously published algorithm [55]. ROIs were manually selected and pixels were averaged for each frame within each ROI. ROI traces were converted to ΔF/F_0 by estimating F_0 as the 12th percentile in an 800 ms sliding window. Drift was assessed by computing the Pearson correlation between trial-averaged calcium traces for each ROI at all possible lags. Correlation values from the same lag (e.g. between Day 1 and 2, Day 2 and 3) were averaged for each ROI (a similar procedure was used for the multi-unit data comparison in Fig. 6b). To account for any uncertainty in the alignments due to the 30 Hz sampling rate of the camera, we then

computed the maximum Pearson correlation in a 100 ms window. Drift was then quantified using a randomization permutation test with a p=.01 threshold. Specifically, we compared the correlations observed at each lag (1–4 days) with correlations from the same data with the group (i.e. day) labels scrambled. P-values were determined by estimating the probability that the observed correlation was greater than or equal to the correlation values from over 10,000 randomizations. We also repeated this analysis using the timing of peak ΔF/F_0 on each day (not shown). Specifically, for each ROI the time of peak trial-averaged ΔF/F_0 was computed on each day, and the peak times were compared between each day of imaging and the first. For each cell, if the peak timing changed by more than 100 ms or there were no peaks greater than .5% ΔF/F_0, the cell was considered unstable.

In order to compare within-day to overnight changes in correlations, we split the data on each day in halves by trial number. The within-day correlations were measured by computing the correlations between trial-averages using the first and second half of trials from a given day. The overnight correlations were measured by computing the correlations between trial-averages from the second half of one day with the first half of the subsequent day. The within-day and overnight correlations were averaged across days for each ROI, and subsequently a Wilcoxon signed-rank test was used to compare the two groups of correlation values. For visualization (Fig. 6c) the two populations were Z-scored using a bootstrap.

To test for significant interactions between time of day and the consistency of calcium activity, we first computed the amplitude of peak ΔF/F_0 across the entire song for each ROI (this controlled for any change in song duration across the day). Next, we computed the standard deviation of the peak ΔF/F_0 in 1 hour bins and computed the Spearman rank correlation between these values and time of day. To account for changes in peak ΔF/F_0 due to photobleaching, we computed the partial rank correlation between the time of day and standard deviation of the peak ΔF/F_0 after accounting for the correlation between time of day and mean of the peak ΔF/F_0 (again using 1 hour bins). Then, to analyze the similarity of calcium activity to the previous day's average, we peak-normalized the ΔF/F_0 values for each trial through dividing by the median peak ΔF/F_0 determined using the 5 nearest trials (with respect to time of day). Then, we estimated the similarity between each trial and the previous day's average using the peak Pearson correlation coefficient (also over a 100 ms window). Finally, we computed the Spearman rank correlation between these similarity values and time of day.

Controls for stability of the imaging plane and photobleaching—Across days, ROIs were manually inspected and adjusted to insure that the center of mass for each ROI was at the center of the ROI mask, and that the mask did not overlap with neighboring cells. Masks that were moved more than the diameter of the mask at any point of the longitudinal study were excluded from analysis. To ensure that our results were not impacted by the stability of the imaging plane, we then checked to see if there were any differences in the spatial profile of stable and unstable ROIs. More precisely, we computed the ΔF/F_0-weighted centroid within each ROI for each day. Then, we took the Euclidean distance between the ΔF/F_0-weighted centroids for each ROI across adjacent days of imaging. Lastly, the distances for unstable and stable ROIs (determined using the permutation test described above) were compared on each day of imaging (e.g. the same ROI imaged on 4

days there would be 3 distances measured from day to day) and we found no significant effect (ROIs$_{present\ some\ days}$ p=.17 z=.97 n=164 and n=620 comparisons made for stable and unstable, respectively, ROIs$_{present\ all\ days}$ p=.99 z=−4.86 n=84 and n=180 comparisons for stable and unstable, respectively; one-tailed Wilcoxon rank-sum test). This indicates that micro-motion of cells in the imaging plane does not correlate with their shift in firing patterns. Moreover, to control for any effects of bleaching in our time of day analysis we repeated the analysis of calcium activity consistency using the Spearman rank partial correlation accounting for correlation between time of day and average peak ΔF/F_0. A significant effect was still observed (ROIs$_{present\ some\ days}$ r=.12 p=7.8e-7 n=1769, ROIs$_{present\ all\ days}$ r=.17 p=2.8e-6, n=708).

Statistical analysis—No formal methods were used to predetermine sample sizes, the sample sizes used here are similar to those used in the field. No randomization of experimental sessions was performed, and no blinding to experiment condition was performed during the analysis. All statistical comparisons were performed using non-parametric tests (Wilcoxon rank-sum, Wilcoxon signed-rank, bootstrap, or randomization tests). Where appropriate, we controlled for multiple comparisons using the Holm-Bonferroni step-down procedure.

Data Availability—The data that support the findings of this study are available from the corresponding author upon request. The latest version of the custom MATLAB scripts used for analysis in this manuscript are available at https://github.com/gardner-lab/HVC-Stability-Analysis.

Supplementary Material

Refer to Web version on PubMed Central for supplementary material.

Acknowledgments

This work was supported by CELEST, an NSF Science of Learning Center CELEST (SBE-0354378) by NINDS (R01-NS089679-01) and by NINDS (1U01NS090454-01). The authors would like to thank H. Eichenbaum and the Center for Neuroscience at BU for the loan of the Inscopix microscope, Special thanks to D. S. Kim and L.Looger for providing the GCaMP6 DNA, and the GENIE project at Janelia Farm Research Campus, Howard Hughes Medical Institute.

References

1. Thompson LT, Best PJ. Long-term stability of the place-field activity of single units recorded from the dorsal hippocampus of freely behaving rats. Brain Res. 1990; 509:299–308. [PubMed: 2322825]
2. Kentros CG, Agnihotri NT, Streater S, Hawkins RD, Kandel ER. Increased attention to spatial context increases both place field stability and spatial memory. Neuron. 2004; 42:283–295. [PubMed: 15091343]
3. Ghosh KK, et al. Miniaturized integration of a fluorescence microscope. Nat. Methods. 2011; 8:871–878. [PubMed: 21909102]
4. Chen T-W, et al. Ultrasensitive fluorescent proteins for imaging neuronal activity. Nature. 2013; 499:295–300. [PubMed: 23868258]
5. Ziv Y, et al. Long-term dynamics of CA1 hippocampal place codes. Nat. Neurosci. 2013; 16:264–266. [PubMed: 23396101]

6. Huber D, et al. Multiple dynamic representations in the motor cortex during sensorimotor learning. Nature. 2012; 484:473–478. [PubMed: 22538608]
7. Leonardo A. Degenerate coding in neural systems. J. Comp. Physiol. A Neuroethol. Sens. Neural. Behav. Physiol. 2005; 191:995–1010. [PubMed: 16252121]
8. Rokni U, Richardson AG, Bizzi E, Seung HS. Motor learning with unstable neural representations. Neuron. 2007; 54:653–666. [PubMed: 17521576]
9. Ganguly K, Carmena JM. Emergence of a stable cortical map for neuroprosthetic control. PLoS Biology. 2009; 7:e1000153. [PubMed: 19621062]
10. Immelmann K. Song development in the zebra finch and other estrildid finches. Bird vocalizations. 1969
11. Lombardino AJ, Nottebohm F. Age at deafening affects the stability of learned song in adult male zebra finches. J. Neurosci. 2000; 20:5054–5064. [PubMed: 10864963]
12. Akutagawa E, Konishi M. New brain pathways found in the vocal control system of a songbird. The Journal of Comparative Neurology. 2010; 518(15):3086–3100. [PubMed: 20533361]
13. Hahnloser RHR, Kozhevnikov AA, Fee MS. An ultra-sparse code underlies the generation of neural sequences in a songbird. Nature. 2002; 419:65–70. [PubMed: 12214232]
14. Kozhevnikov AA, Fee MS. Singing-Related Activity of Identified HVC Neurons in the Zebra Finch. Journal of Neurophysiology. 2007; 97:4271–4283. [PubMed: 17182906]
15. Guitchounts G, Markowitz JE, Liberti WA, Gardner TJ. A carbon-fiber electrode array for long-term neural recording. Journal of Neural Engineering. 2013; 10:046016. [PubMed: 23860226]
16. Markowitz JE, et al. Mesoscopic patterns of neural activity support songbird cortical sequences. PLoS Biology. 2015; 13:e1002158. [PubMed: 26039895]
17. Kosche G, Vallentin D, Long MA. Interplay of inhibition and excitation shapes a premotor neural sequence. J. Neurosci. 2015; 35:1217–1227. [PubMed: 25609636]
18. Lynch GF, Okubo TS, Hanuschkin A, Hahnloser RHR, Fee MS. Rhythmic Continuous-Time Coding in the Songbird Analog of Vocal Motor Cortex. Neuron. 2016; 90:877–892. [PubMed: 27196977]
19. Crandall SR, Aoki N, Nick TA. Developmental modulation of the temporal relationship between brain and behavior. Journal of Neurophysiology. 2007; 97:806–816. [PubMed: 17079340]
20. Otchy TM, et al. Acute off-target effects of neural circuit manipulations. Nature. 2015; 528:358–363. [PubMed: 26649821]
21. Katzner S, et al. Local origin of field potentials in visual cortex. Neuron. 2009; 61:35–41. [PubMed: 19146811]
22. Buzsáki G, Anastassiou CA, Koch C. The origin of extracellular fields and currents - EEG, ECoG, LFP and spikes. Nature Reviews Neuroscience. 2012; 13:407–420. [PubMed: 22595786]
23. Schmidt M. Pattern of Interhemispheric Synchronization in HVc During Singing Correlates With Key Transitions in the Song Pattern. Journal of Neurophysiology. 2003
24. Vallentin D, Long MA. Motor origin of precise synaptic inputs onto forebrain neurons driving a skilled behavior. J. Neurosci. 2015; 35:299–307. [PubMed: 25568122]
25. Nordeen KW, Nordeen EJ. Auditory feedback is necessary for the maintenance of stereotyped song in adult zebra finches. Behav. Neural Biol. 1992; 57:58–66. [PubMed: 1567334]
26. Tschida KA, Mooney R. Deafening drives cell-type-specific changes to dendritic spines in a sensorimotor nucleus important to learned vocalizations. Neuron. 2012; 73:1028–1039. [PubMed: 22405211]
27. Williams H, Crane LA, Hale TK, Esposito MA, Nottebohm F. Right-side dominance for song control in the zebra finch. J. Neurobiol. 1992; 23:1006–1020. [PubMed: 1460461]
28. Picardo MA, et al. Population-Level Representation of a Temporal Sequence Underlying Song Production in the Zebra Finch. Neuron. 2016; 90:866–876. [PubMed: 27196976]
29. Long MA, Jin DZ, Fee MS. Support for a synaptic chain model of neuronal sequence generation. Nature. 2010; 468:394–399. [PubMed: 20972420]
30. Weinstein GD, van Scott EJ. Autoradiographic Analysis of Turnover Times of Normal and Psoriatic Epidermis1. Journal of Investigative Dermatology. 1965; 45:257–262. [PubMed: 5837896]

31. Creamer B, Shorter RG, Bamforth J. The turnover and shedding of epithelial cells Part I The turnover in the gastro-intestinal tract. Gut. 1961; 2:110–116. [PubMed: 13696345]
32. Diesmann M, Gewaltig MO, Aertsen A. Stable propagation of synchronous spiking in cortical neural networks. Nature. 1999; 402:529–533. [PubMed: 10591212]
33. Mooney R, Prather JF. The HVC Microcircuit: The Synaptic Basis for Interactions between Song Motor and Vocal Plasticity Pathways. J. Neurosci. 2005; 25:1952–1964. [PubMed: 15728835]
34. Amador A, Perl YS, Mindlin GB, Margoliash D. Elemental gesture dynamics are encoded by song premotor cortical neurons. Nature. 2013; 495:59–64. [PubMed: 23446354]
35. Cannon J, Kopell N, Gardner T, Markowitz J. Neural Sequence Generation Using Spatiotemporal Patterns of Inhibition. PLoS Comp Bio. 2015; 11:e1004581.
36. Rubino D, Robbins KA, Hatsopoulos NG. Propagating waves mediate information transfer in the motor cortex. Nat. Neurosci. 2006; 9:1549–1557. [PubMed: 17115042]
37. Murthy VN, Fetz EE. Coherent 25- to 35-Hz oscillations in the sensorimotor cortex of awake behaving monkeys. Proceedings of the National Academy of Sciences of the United States of America. 1992; 89:5670–5674. [PubMed: 1608977]
38. Dombeck DA, Graziano MS, Tank DW. Functional clustering of neurons in motor cortex determined by cellular resolution imaging in awake behaving mice. J. Neurosci. 2009; 29:13751–13760. [PubMed: 19889987]
39. Peters AJ, Chen SX, Komiyama T. Emergence of reproducible spatiotemporal activity during motor learning. Nature. 2014
40. Hira R, et al. Spatiotemporal dynamics of functional clusters of neurons in the mouse motor cortex during a voluntary movement. J. Neurosci. 2013; 33:1377–1390. [PubMed: 23345214]
41. Ohgushi E, Mori C, Wada K. Diurnal oscillation of vocal development associated with clustered singing by juvenile songbirds. J. Exp. Biol. 2015; 218:2260–2268. [PubMed: 26034125]
42. Deregnaucourt S, Mitra PP, Feher O, Pytte C, Tchernichovski O. How sleep affects the developmental learning of bird song. Nature. 2005; 433:710–716. [PubMed: 15716944]
43. Crick F, Mitchison G. The function of dream sleep. Nature. 1983
44. Dave AS, Margoliash D. Song replay during sleep and computational rules for sensorimotor vocal learning. Science. 2000; 290:812–816. [PubMed: 11052946]
45. Wilson AA, et al. Sustained expression of alpha1-antitrypsin after transplantation of manipulated hematopoietic stem cells. Am. J Respir. Cell Mol. Biol. 2008; 39:133–141. [PubMed: 18323534]
46. Fee MS, Leonardo A. Miniature motorized microdrive and commutator system for chronic neural recording in small animals. Journal of Neuroscience Methods. 2001; 112:83–94. [PubMed: 11716944]
47. Poole B, Markowitz JE, Gardner TJ. The song must go on: resilience of the songbird vocal motor pathway. PloS one. 2012; 7:e38173. [PubMed: 22768040]
48. Markowitz JE, Ivie E, Kligler L, Gardner TJ. Long-range order in canary song. PLoS Comp Bio. 2013; 9:e1003052.
49. Lim Y, Shinn-Cunningham B, Gardner TJ. Stable Time-Frequency Contours for Sparse Signal Representation. EUSIPCO. 2013:1–5.
50. Aoi M, Lepage K, Lim Y, Eden UT, Gardner TJ. An Approach to Time-Frequency Analysis With Ridges of the Continuous Chirplet Transform. Signal Processing, IEEE Transactions on. 2015; 63:699–710.
51. Tchernichovski O, Nottebohm F, Ho C, Pesaran B, Mitra P. A procedure for an automated measurement of song similarity. Anim Behav. 2000; 59:1167–1176. [PubMed: 10877896]
52. Sahani, M. PhD Thesis. Pasadena, CA: California Institute of Technology; 1999. Latent variable models for neural data analysis.
53. Tolias AS, et al. Recording chronically from the same neurons in awake, behaving primates. Journal of Neurophysiology. 2007; 98:3780–3790. [PubMed: 17942615]
54. Quiroga RQ, Nadasdy Z, Ben-Shaul Y. Unsupervised spike detection and sorting with wavelets and superparamagnetic clustering. Neural Computation. 2004; 16:1661–1687. [PubMed: 15228749]
55. Guizar-Sicairos M, Thurman ST, Fienup JR. Efficient subpixel image registration algorithms. Opt Lett. 2008; 33:156–158. [PubMed: 18197224]

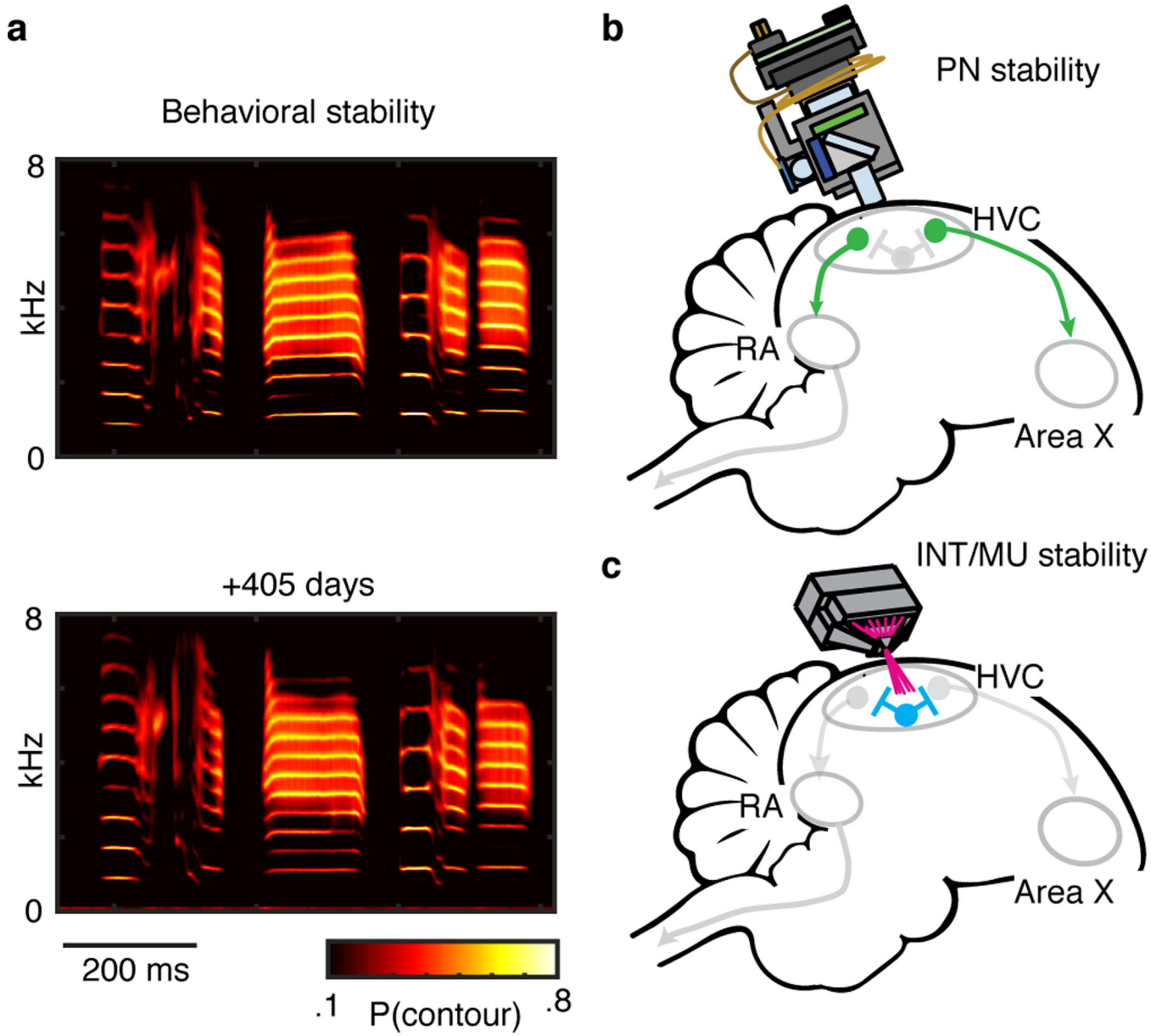

Figure 1. Approach to measuring the stability of neural firing patterns underlying a highly stable behavior

A, Spectral density images (see **Methods**) for the songs sung by the same bird 405 days apart (n=1412 songs for Day 1 and n=1480 songs for Day 405, audio recordings performed in n=10 birds). **B**, To measure projection neuron stability a head mounted fluorescence microscope was used to image GCaMP6 delivered by a cell-type specific virus. **C**, Stability of multi-unit and inhibitory interneuron activity patterns was measured using a custom carbon fiber electrode array (see **Methods**).

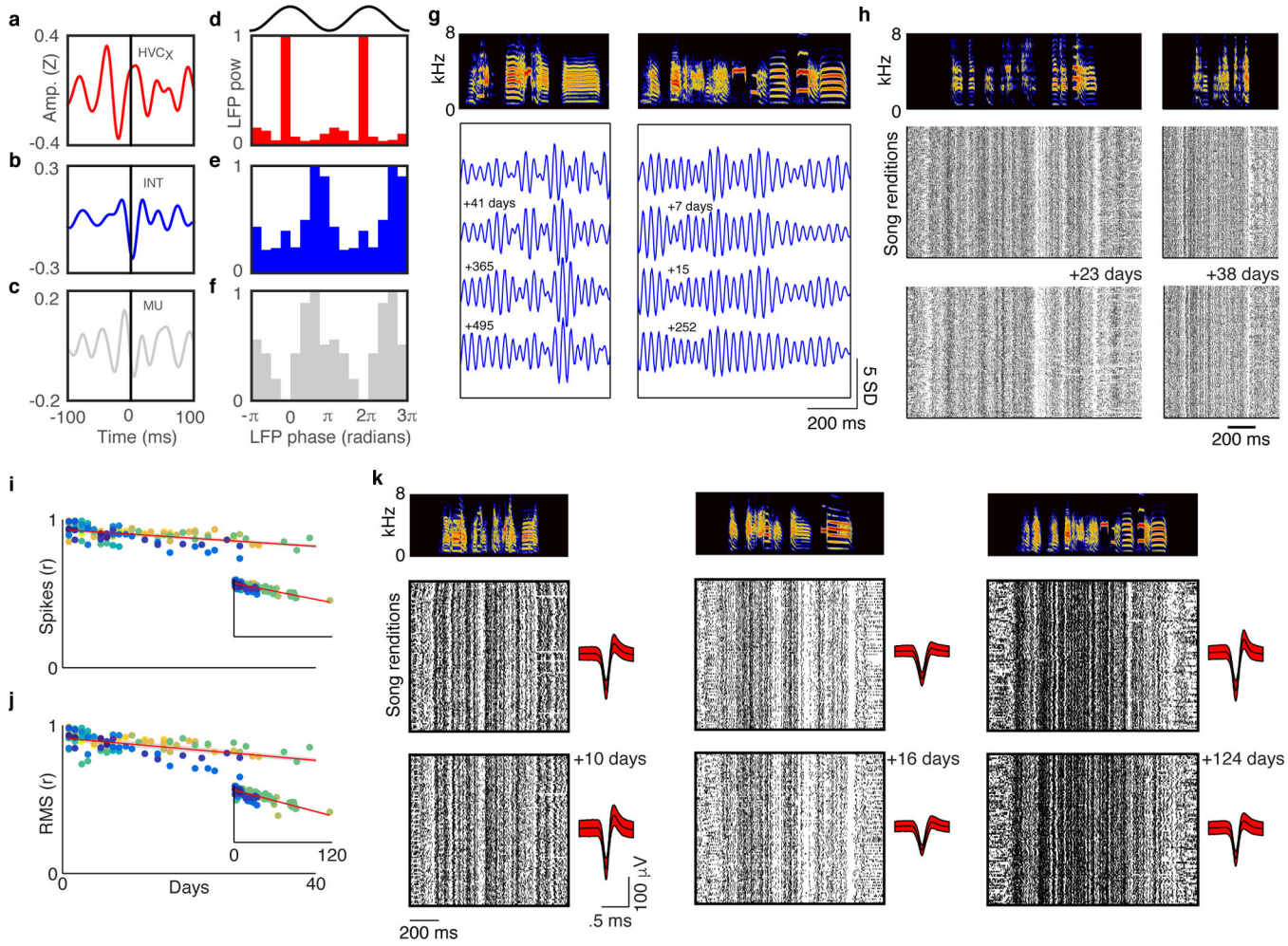

Figure 2. Activity patterns from multi-unit ensembles and single interneurons are highly stable

A–C, Burst-triggered averages of 25–35 Hz Local Field Potentials (LFPs) for HVC_X neurons (average of n=12 neurons) (**A**), interneurons (average of n=65 neurons) (**B**), and multi-unit activity (average of n=3 sites with both multi-unit and LFP recordings) (**C**). **D–F**, Histogram where the power of the LFP is binned at the phase of the LFP for each burst time. A clear separation in preferred phase can be seen between HVC_X neurons (histogram from n=12 neurons) (**D**) and interneurons (histogram from n=65 neurons) (**E**), but not between interneurons and multiunit activity (n=3 sites with both multi-unit and LFP recordings) (**F**). **G**, Two examples of trial-averaged band-passed LFPs (25–35 Hz) from a single electrode in two different birds. Here the LFP is trial-averaged on each day of the recording (LFP recordings repeated across n=182 channels from n=21 birds). The left example was recorded up to 495 days post-implant. **H**, Examples of multiunit stability over month-long timescales (multi-unit recorded from n=20 sites). **I–J**, Multi-unit patterns are stable over 40 days measured using patterns in firing rate (regression slope −.0028) (**I**) or root-mean-square (RMS) (regression slope −.0038) (**J**) values are stable over 40 days (inset, over 120 days). Shown are average correlations between each day and the first day, red line indicates linear regression and shading indicates 99% confidence interval of fitted values (n=130 values from n=20 birds). Colors indicate different birds, many are not visible due to overlap in the

upper-left portion of the plot. **K**, Three example inhibitory interneuron firing patterns (of n=6 recordings lasting more than 24 hours). The right-most example is stable for up to 124 days. Average waveforms from each day are shown next to the corresponding raster, red shading indicates standard deviation.

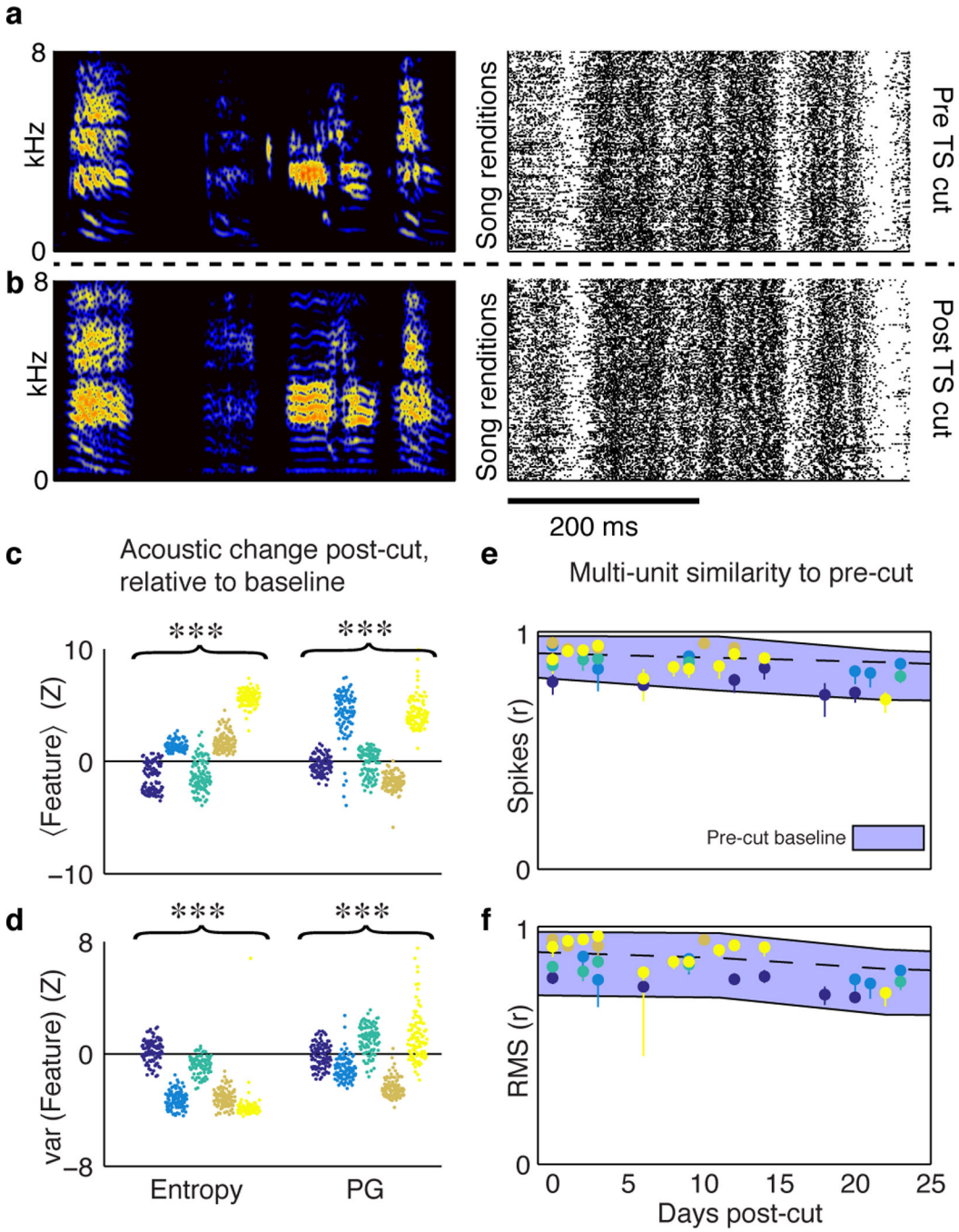

Figure 3. Drift in multi-unit firing patterns is not accelerated by unilateral TS nerve transaction

A–B, Representative sonogram and multiunit raster before (**A**) and after the TS nerve cut (**B**) (experiment performed in n=5 birds). **C–D**, Change in acoustic features after nerve cut (***, p<.001, Wilcoxon rank-sum test, ⟨Entropy⟩ p=1.9e-15 z=−7.95, ⟨PG⟩ p=5.7e-5 z=−4.02, var(Entropy) p=0 z=16.25, var(PG) p=2.6-e5 z=4.21, n=100 songs each from n=5 birds, see **Methods**). **E–F**, Post-nerve cut, multi-unit activity does not drift more than expected in the pre-cut baseline condition (n=34 timepoints from n=5 birds). Shown is the average

correlation at each time point relative to the last baseline day. Blue indicates the 99% bootstrap confidence interval estimated from the baseline condition.

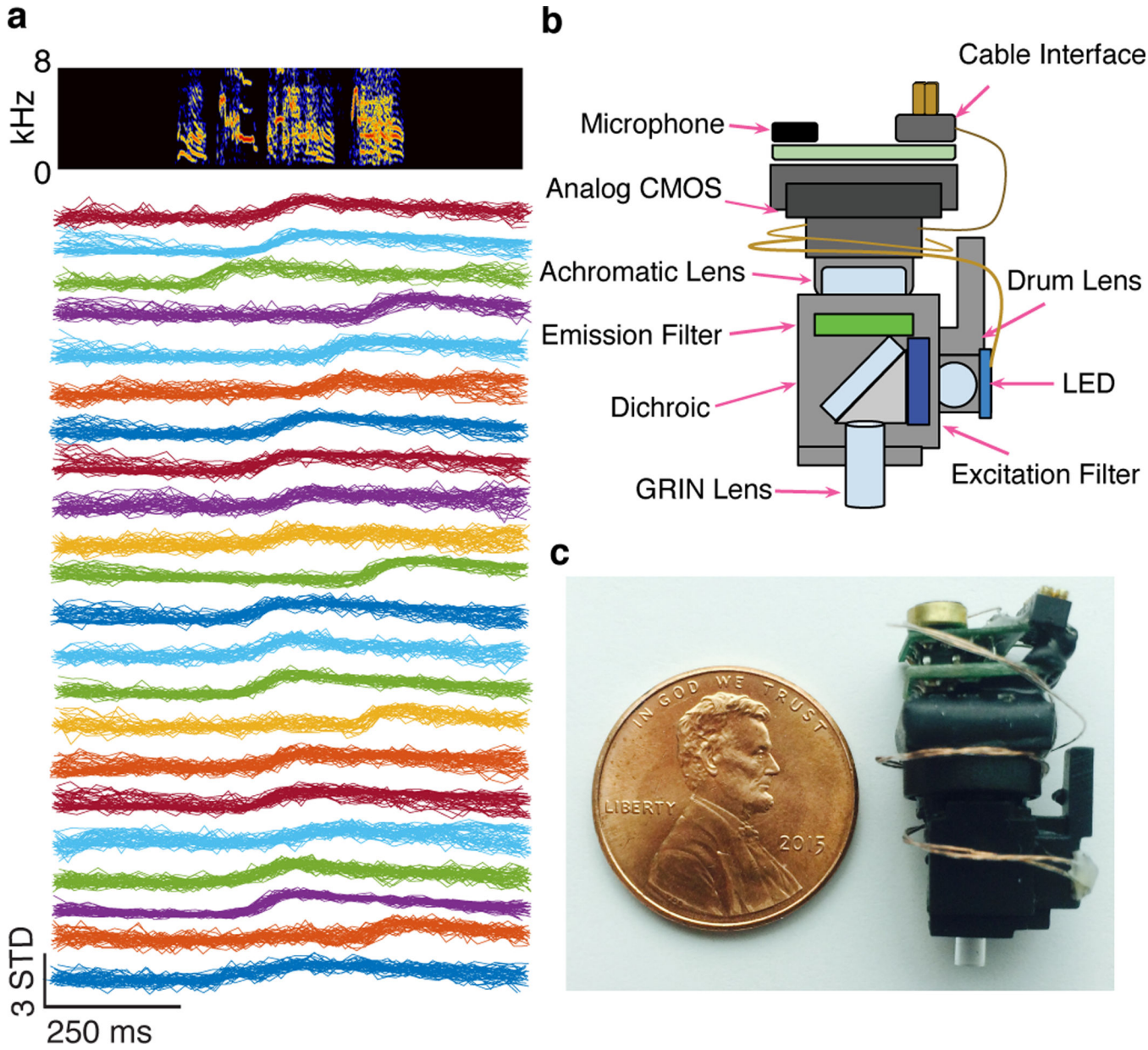

Figure 4. A custom head-mounted fluorescence microscope adapted for use in singing birds

A, Calcium traces from 22 ROIs over 50 song-aligned trials in a single bird (imaging performed in n=4 birds). **B**, Schematic of the miniature microscope used for this study (see **Methods**). **C**, Photograph of the 3D printed microscope.

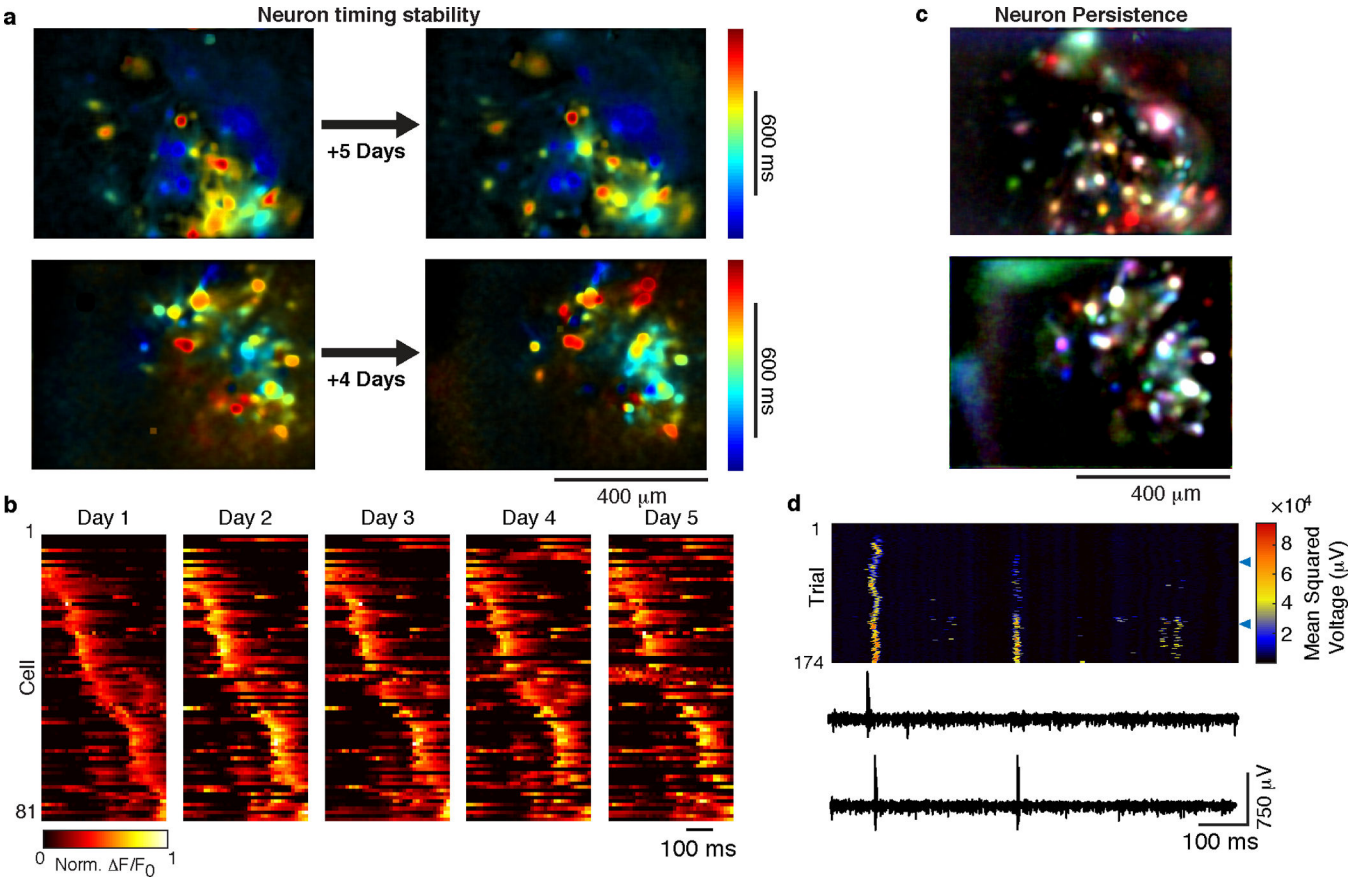

Figure 5. Projection neurons drift over a five day imaging session

A, Images colored by the timing of max pixel intensity, for two birds, across 5 (top, commercial microscope) and 4 (bottom, custom microscope) day intervals (imaging performed in n=4 birds). **B**, Trial-averaged activity from all song related neurons from one animal. Keeping the same sorting and amplitude color scale, the ROIs are plotted for 5 consecutive days. **C**, For the same animals shown in **A**, cells active on three consecutive days are combined in a single image where color now indicates neuron participation rather than timing. (red=day 1, blue=day 2, and green=day 3). Cells with persistent activity on all 3 days appear white in this representation (see Supplementary Figure 5). Cells that change amplitude or change firing probability appear colored. **D**. Electrophysiological recording of a projection neuron reveals a new song-locked burst that emerges over the course of a day. Blue triangles indicate trials plotted at the bottom of the figure.

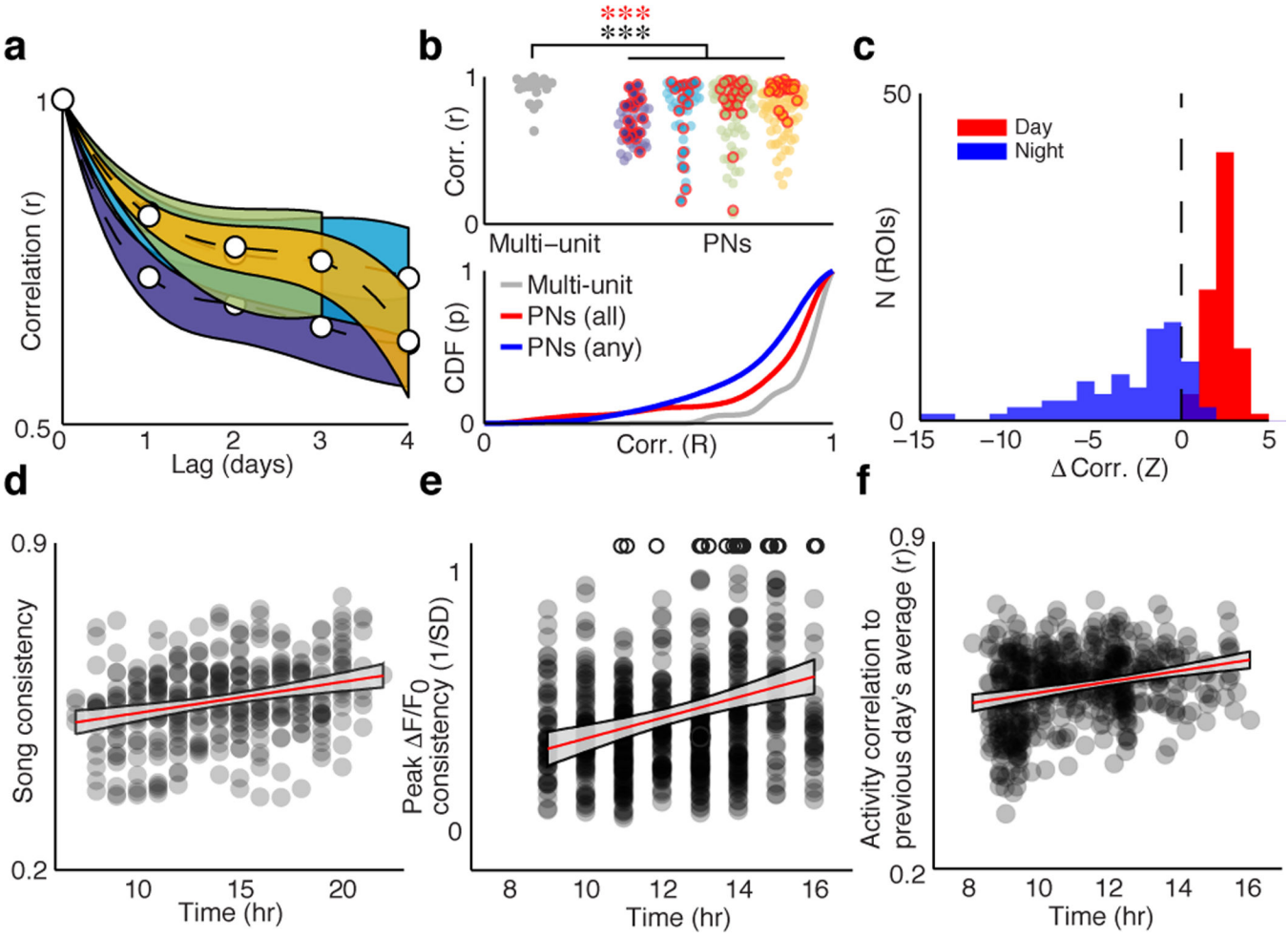

Figure 6. Projection neuron activity preferentially changes over periods of sleep

A, Average correlation across all ROIs across different lags for each bird. Shaded region indicates 99% bootstrap confidence interval (ROIs$_{present\ some\ days}$). **B**, *Top*, All correlations up to a lag of 4 days for multi-unit activity (n=20 birds, one sample per bird) and projection neuron activity (ROIs$_{present\ some\ days}$, p=2.7e-6, z=4.70, one-tailed Wilcoxon rank-sum test, n=234 ROIs from n=4 birds). Highlighted in red are cells that participate unambiguously across the entire time series (ROIs$_{present\ all\ days}$, p=9.8e-4, z=3.30 one-tailed Wilcoxon rank-sum test, n=77 ROIs from n=4 birds). *Bottom*, Cumulative density functions (CDF) of the data shown above: multiunit data in gray, projection neurons seen across all days in red, and seen clearly on any day are blue. **C**, The shift in correlation occurs primarily overnight (***, ROIs$_{present\ some\ days}$ p=2.0e-40, z=−13.26, ROIs$_{present\ all\ days}$ p=1.6e-14, z=−7.59, Wilcoxon signed-rank test; shown are data from ROIs$_{present\ all\ days}$). **D**, Song consistency increases over the course of the day (r=.28, p=6.6e-8, Spearman rank correlation, n=372 values from n=10 birds, see **Methods**). **E**. Consistency in the timing of peak ΔF/F_0 (measured over the whole song) increases with time of day (ROIs$_{present\ some\ days}$ r=.14 p=6.1e-9 n=1769 values, ROIs$_{present\ all\ days}$ r=.18 p=9.7e-7 n=708 values, Spearman rank correlation, see **Methods**; shown are data from ROIs$_{present\ all\ days}$). **F**. The trial by trial correlation between calcium activity and the previous day's average also increases with time of day (ROIs$_{present\ some\ days}$

r=.12 p=5.6e-3 n=529 values, ROIs$_{present\ all\ days}$ r=.25 p=4.3e-9 540 values, Spearman rank correlation; shown are data from ROIs$_{present\ all\ days}$). All time of day measurements in **E** and **F** use only data our custom microscopes detailed in Fig. 4 (n=3 birds, n=153, ROIs$_{present\ some\ days}$, n=56 ROIs$_{present\ all\ days}$). For all linear regressions shown (red lines in **D–F**), shading indicates 99% confidence interval of the fitted values,